INORGANIC CHEMISTRY
FRONTIERS

RESEARCH ARTICLE

View Article Online
View Journal | View Issue

Cite this: *Inorg. Chem. Front.*, 2021, **8**, 2461

Three-dimensional porous copper-decorated bismuth-based nanofoam for boosting the electrochemical reduction of CO_2 to formate†

Yingchun Zhang,[a,b] Changsheng Cao, *[a,b] Xin-Tao Wu [a,b,c] and Qi-Long Zhu *[a,b,c]

Received 15th January 2021,
Accepted 17th March 2021

DOI: 10.1039/d1qi00065a

rsc.li/frontiers-inorganic

Bismuth (Bi)-based nanomaterials are considered as promising electrocatalysts for the electrocatalytic CO_2 reduction reaction (CO_2RR), but it is still challenging to achieve high current density and selectivity in a wide potential window. Herein, Cu-decorated Bi/Bi_2O_3 nanofoam (P–Cu–BiNF) with a 3D porous network structure was prepared for the first time *via* a simple fast-reduction method. Characterizations indicate that the introduction of Cu can significantly regulate the microstructure and electronic states of Bi/Bi_2O_3. Consequently, the as-prepared P–Cu–BiNF exhibits excellent electrocatalytic performance toward the CO_2RR. Remarkably, the faradaic efficiency of formate production can exceed 90% in a wide potential range from –0.78 to –1.08 V. Meanwhile, it can also deliver a high formate partial current density of up to 62.7 mA cm^{-2} at –1.18 V and long-term stability. This work provides a simple but effective way to synthesize advanced Bi-based materials with significantly improved electrocatalytic CO_2RR performance.

1. Introduction

Conversion of CO_2 into valuable fuels and chemicals through the electrocatalytic CO_2 reduction reaction (CO_2RR) represents a promising way to solve the energy and environmental problems caused by the gradually rising CO_2 concentration in the atmosphere (*i.e.* the greenhouse effect).[1–5] Among the various products produced through the CO_2RR, formic acid/formate is an attractive one, not only for its favorable 2-electron thermodynamic process,[6] but also for its high economic values in energy and chemical manufacturing.[7–11]

Substantial experimental and theoretical efforts have revealed that Bi-,[12–16] Sn-,[17,18] Pb-,[19,20] In-,[21,22] and Pd-based[23] CO_2RR electrocatalysts favour the production of formate in aqueous electrolytes. In particular, the Bi-based materials stand out, not only for their low toxicity and cost, and high stability,[12,13] but also for their intrinsically unfavourable hydrogen evolution reaction (a competing reaction of the CO_2RR), weak adsorption energy of CO and strong stabilizing ability for the key OCHO* intermediate for formate generation.[24,25] However, few of them can simultaneously meet the requirements of high current density, selectivity and stability in wide potential windows.[26] Therefore, it is urgent but challenging to develop high-performance Bi-based electrocatalysts to achieve the desirable formic acid/formate production.

Besides the morphology engineering strategy,[27,28] the development of multicomponent electrocatalysts is another fascinating way to achieve the target electrocatalytic performance, since the synergistic effect between each component always brings unexpected improvements in the electrocatalytic properties in comparison with their single counterparts.[29–32] For metal-based CO_2RR electrocatalysts, rational introduction of a secondary element could significantly improve their activity and selectivity *via* the modulation of their electronic structures. For instance, Ren *et al.* reported that the introduction of Zn can modify CO binding over the Cu sites in a CuZn bimetallic catalyst, thus enabling much improved selectivity toward electroreduction of CO_2 to ethanol.[33] Very recently, Shen *et al.* discovered that the strong interaction between Fe and Au atoms in single-atom Fe-incorporated Au crystals can affect the adsorption of reaction intermediates, thus achieving much improved selectivity and mass activity for the electrochemical CO_2RR to CO.[34] When focused on Bi-based materials, Zeng, Geng and co-workers reported that covering Bi nanoparticles with an outer Sn shell can boost the activity and selectivity toward electroreduction of CO_2 to formate.[35] In another study, Yang *et al.* attempted to modulate the local electronic state of Bi nanocrystals through

[a]*State Key Laboratory of Structural Chemistry, Fujian Institute of Research on the Structure of Matter, Chinese Academy of Sciences (CAS), Fuzhou 350002, China. E-mail: cscao@fjirsm.ac.cn, qlzhu@fjirsm.ac.cn*
[b]*University of Chinese Academy of Sciences, Beijing 100049, China*
[c]*Fujian Science & Technology Innovation Laboratory for Optoelectronic Information of China, Fuzhou 350108, China*
†Electronic supplementary information (ESI) available. See DOI: 10.1039/d1qi00065a

Cu incorporation, which would alter the pathway for formate formation.[26] However, despite numerous efforts having been made, few of them can simultaneously regulate the microstructure and the local electronic environment of Bi in a simple way, which would result in desirable CO_2-to-formate conversion performance.

Herein, we demonstrated that porous Cu-decorated Bi/Bi_2O_3 nanofoam (P–Cu–BiNF), which was prepared through a sodium borohydride ($NaBH_4$)-assisted fast-reduction method, could serve as a high-performance CO_2RR electrocatalyst to trigger the conversion of CO_2-to-formate. It is interesting that the as-prepared P–Cu–BiNF features a 3D porous network architecture composed of interconnected nanoparticles with a uniform size of around 15–20 nm. Further characterizations indicated that the incorporation of Cu can significantly regulate the micromorphology, crystallinity and local electron state of Bi/Bi_2O_3. With the rational control of the introduced amount of Cu, the as-prepared P–Cu–BiNF can deliver high partial current density (62.7 mA cm^{-2} at −1.18 V) and long-term stability, as well as a high faradaic efficiency (>90%) in a wide potential range from −0.78 to −1.08 V for formate production.

2. Experimental

2.1 Chemicals

$Bi(NO_3)_3{\cdot}5H_2O$ (99.0%), $Cu(NO_3)_2{\cdot}3H_2O$, (99.0%), $NaBH_4$ (98%), $KHCO_3$ (99.5%), *tert*-Butanol (99.0%) and isopropanol (99.7%) were purchased from Sinopharm Chemical Reagent Co. Ltd (Shanghai, China). Nafion solution (5 wt%) was purchased from Alfa Aesar. Dimethylsulfoxide (DMSO, 99.95%) was purchased from Aladdin Reagent. All reagents were of analytical grade and used without further purification. Deionized water was used during all experiments.

2.2 Synthesis of P–Cu–BiNF

P–Cu–BiNF was prepared as follows: the metal precursor solution containing Bi^{3+} and Cu^{2+} was quickly poured into a freshly prepared $NaBH_4$ solution, and underwent vigorous stirring at room temperature. Then the black product was collected and washed with deionized water several times. Afterwards, the samples were soaked in *tert*-butanol for 24 h and freeze dried for 12 h in sequence. The finally obtained samples were named as P–Cu–BiNF-x (x = 0.5, 5 or 10), where x is the molar ratio of Bi^{3+} : Cu^{2+} in the metal precursors. Without specific explanation, the sample named P–Cu–BiNF in this work represents P–Cu–BiNF-5. For comparison, the samples P–Bi and P–Cu were prepared with a similar procedure to that of P–Cu–BiNF-x, except that Cu^{2+} or Bi^{3+} was not added, respectively.

2.3 Physical characterization

The powder X-ray diffraction (PXRD) patterns of the samples were measured on a Rikagu Miniflex 600 Benchtop X-ray diffraction instrument with Cu Kα radiation. Scanning electron microscopy (SEM) characterization was performed on a Carl Zeiss Sigma 300 instrument. Transmission electron microscopy (TEM) and high-resolution TEM (HRTEM) images of the samples were obtained using an FEI Tecnai G2 F30 instrument. A Ti TEM grid was used as the sample carrier. The Raman spectra were recorded in a LabRAM HR Raman microscope with a 633 nm laser. X-ray photoelectron spectroscopy (XPS) analysis was performed on a Thermo Fischer ESCALAB 250Xi X-ray photoelectron spectrometer with monochromatic Al Kα radiation (E = 1486.2 eV), and the binding energies were calibrated by C 1s to 284.8 eV.

2.4 Electrochemical characterization

CO_2RR measurements were performed in a proton exchange membrane (Nafion 117) separated H-type cell connected to an electrochemical workstation (CHI 760), in which a Pt mesh was used as the counter electrode and saturated Ag/AgCl was used as the reference electrode. Electrocatalyst-coated carbon paper with a size of 1.0 × 1.0 cm^2 was used as the working electrode. To prepare the working electrode, 5 mg of sample was dispersed in 1.0 mL of mixed solvent containing 500 μL of H_2O, 450 μL of isopropanol and 50 μL of 5 wt% Nafion with ultrasonic treatment for 1 h. Then, 50 μL of the ink was successively dropped onto both sides of carbon paper with a size of 1.0 × 1.0 cm^2 and naturally dried at room temperature to get a mass loading of 0.5 mg cm^{-2}. CO_2-saturated 0.5 M $KHCO_3$ was used as the electrolyte. CO_2 with a flow rate of 20.0 sccm was passed through the electrolyte during electrolysis. All the measured potentials were converted to reversible hydrogen electrode (RHE) potentials based on the formula $E_{RHE} = E_{Ag/AgCl} + 0.197 + 0.0591\ pH(v)$. Linear sweep voltammetry (LSV) curves were recorded at a scan rate of 10 mV s^{-1}. Electrochemical impedance spectroscopy (EIS) was performed in the frequency range from 0.1 to 10^5 Hz at the AC amplitude of 5 mV.

2.5 Product analysis

During the CO_2RR process, gas products (CO and H_2) were quantified with gas chromatography (Agilent 7820A), which was equipped with a thermal conductivity detector (TCD) and flame ionization detector (FID). Argon (99.99%) was used as the carrier gas. Liquid products (formate) were quantified by ^1H nuclear magnetic resonance (NMR) spectroscopy. In a typical analysis, a mixture of 0.5 mL of the electrolyte and 0.1 mL of a 10 mM DMSO (used as an internal standard) D_2O solution was used as the measured sample. The ^1H spectra were obtained by using a pre-saturation method to suppress the water peak.

3. Results and discussion

As schematically shown in Fig. 1, P–Cu–BiNF-x was prepared *via* a simple fast-reduction method, in which x is the molar ratio of Bi^{3+} : Cu^{2+} in the metal precursors during the synthesis process and freshly prepared $NaBH_4$ was used as the metal pre-

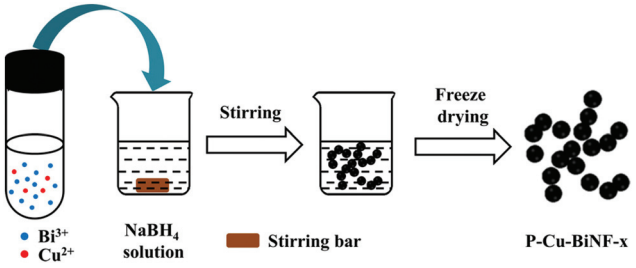

Fig. 1 Schematic diagram of the synthesis of P–Cu–BiNF.

cursor and reducing agent, respectively. Unless otherwise indicated, the sample named P–Cu–BiNF represents the sample P–Cu–BiNF-5 throughout the work. Apparently, the as-prepared P–Cu–BiNF is a fluffy powder-like sample (inset in Fig. 2a). Scanning electron microscopy (SEM) and transmission electron microscopy (TEM) images reveal that P–Cu–BiNF features a 3D porous network architecture, which is composed of interconnected nanoparticles with a uniform size of around 15–20 nm (Fig. 2a–d). In contrast, commercial bulk Bi and P–Bi display the morphologies of micron-sized nanoparticles and irregular porous nanoparticles (Fig. S1†), demonstrating that the unique morphology of P–Cu–BiNF is assigned to the cooperation of the fast-reduction method and the incorporation of Cu. SEM energy-dispersive X-ray (SEM-EDX) analysis indicates that the ratios of Cu in the as-prepared P–Cu–BiNF-*x* are consistent with the amounts of initially added Cu^{2+} (Fig. S2†). However, further studies implied that the different amounts of Cu can deliver similar nanostructures of P–Cu–BiNF-*x* (Fig. S3†). Moreover, the high-resolution TEM (HRTEM) image of P–Cu–BiNF shows the low crystallinity, or even amorphous structure, in most regions of the nanoparticles (Fig. 2e), corresponding to the ring-like pattern of the selected-area electron diffraction (SAED) image (inset in Fig. 2e). The TEM-EDX spectra show that the atomic ratio of Bi : Cu is *ca.* 2 (Fig. S4†). And TEM-mapping reveals the homogeneous distribution of Bi, Cu and O elements in P–Cu–BiNF (Fig. 2f–i). In addition, the SEM-mapping of P–Cu–BiNF-0.5 also proves the uniform distribution of Bi and Cu (Fig. S5†). Notably, the signal of O elements in P–Cu–BiNF should originate from the coexistence of the oxide components. These results demonstrate that the incorporation of Cu into P–Cu–BiNF-*x* can effectively regulate their morphologies and nanostructures.

The influence of the decoration of Cu on the structure of P–Cu–BiNF was further explored. As displayed in Fig. 3a, the typical powder X-ray diffraction (PXRD) peaks of P–Bi can be fully indexed to the standard crystalline phase of Bi with *R*3*c* space group (JCPDS 44-1246),[36] which is similar to that of the bulk Bi. Meanwhile, other weak peaks assigned to Bi_2O_3 can also be detected.[13] However, in comparison with P–Bi, a broad diffraction peak at $2\theta \approx 27.2°$, as well as peaks corresponding to metallic Bi with significantly reduced intensity, are observed for P–Cu–BiNF. And the relatively low Cu content leads to no Cu peaks. As the amount of introduced Cu increases, the intensity of the diffraction peaks obviously decreases (Fig. S6a†), indicating that the incorporation of Cu will significantly reduce the crystallinity of Bi/Bi_2O_3, corresponding to the HRTEM result. X-ray photoelectron spectroscopy (XPS) was employed to study the surface electronic states of P–Bi and P–Cu–BiNF. P–Cu–BiNF is mainly composed of two metal elements, Bi and Cu, of which Cu mainly exists in the form of $Cu^{0/1+}$ and Cu^{2+} (Fig. S6b†).[37] The other major element is Bi, and as displayed in Fig. 3b, the peaks at around 157 and 162 eV match the metallic Bi^0 species,[12] but the intensity of those peaks is quite low or even absent, which could be ascribed to the existence of an oxide layer and the limited detection depth of XPS.[15] Besides, the peaks at around 159 and 164 eV could

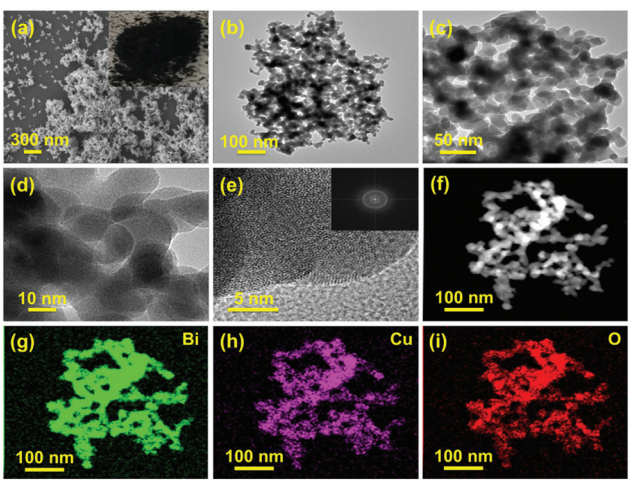

Fig. 2 (a) SEM, (b–d) TEM, (e) HRTEM and (f) HAADF-STEM images and (g–i) TEM-mapping images of P–Cu–BiNF. Insets in (a) and (e) are the optical photo and SAED image of P–Cu–BiNF, respectively.

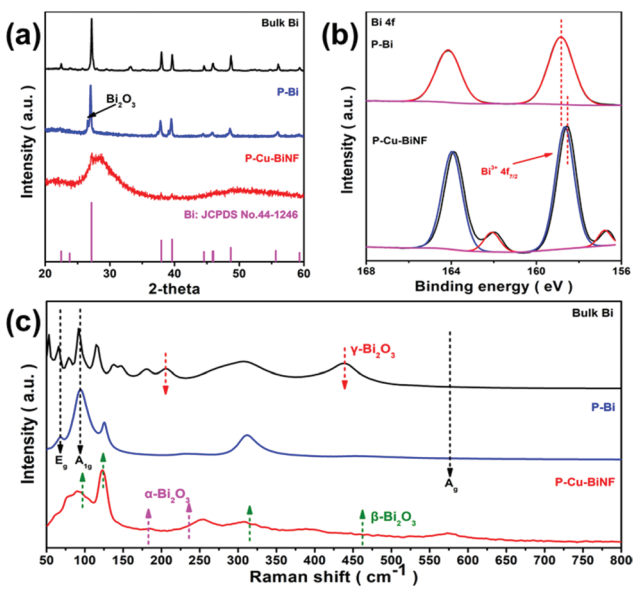

Fig. 3 (a) PXRD patterns, (b) XPS Bi 4f and (c) Raman spectra of P–Cu–BiNF, P–Bi and bulk Bi.

be assigned to Bi^{3+}.[12] Compared with P–Bi, the peaks assigned to Bi^{3+} for P–Cu–BiNF have a negative shift, indicating that the decoration of Cu can regulate the local electronic structure of the Bi, which may be beneficial to improving its CO_2RR performance.[38] In addition, Raman spectroscopy was carried out to measure the composition and structure of P–Cu–BiNF. As shown in Fig. 3c and S6c,† in comparison with P–Bi, the intensity of the peaks at 71 and 91 cm^{-1}, corresponding to the E_g and A_{1g} of the metallic Bi–Bi bond,[39] is sharply decreased and broadened upon the decoration of Cu for P–Cu–BiNF, indicating its amorphization.[40] Meanwhile, the peaks at 95, 123, 307 and 461 cm^{-1} are attributed to the Bi–O stretches in the β-Bi_2O_3 structure.[13,15] More importantly, the position of the peaks at 123 and 307 cm^{-1} is gradually shifted to lower wave numbers on increasing the amount of introduced Cu, reflecting the change in structure and the increase in disorder.[41] Small amounts of α- and γ-Bi_2O_3 are also present here.[13,15] The Brunauer–Emmett–Teller (BET) surface areas and pore size distributions of bulk Bi, P–Bi and P–Cu–BiNF were evaluated by N_2 sorption, as shown in Fig. S7.† The BET surface areas of P–Bi and P–Cu–BiNF are 1.8 and 21.4 $m^2\ g^{-1}$, respectively, and their pore size distribution demonstrates the plentiful meso-/macro-porosity, which could be beneficial for the accessibility of the surface active sites and the mass transport during electrocatalysis.

The electrochemical CO_2RR performances of P–Cu–BiNF, P–Bi and bulk Bi were evaluated using an H-type electrochemical cell in 0.5 M $KHCO_3$ electrolyte. Linear sweeping voltammetry (LSV) curves were firstly recorded under Ar and CO_2 atmospheres. As depicted in Fig. 4a, all samples showed much higher current densities under a CO_2 atmosphere, suggesting that the CO_2RR efficiently occurred.[42] Among the three samples, P–Cu–BiNF can deliver much higher current densities compared with P–Bi and bulk Bi, which may be ascribed to the synergistic effect derived from the ingenious 3D porous network structure and Cu decoration.

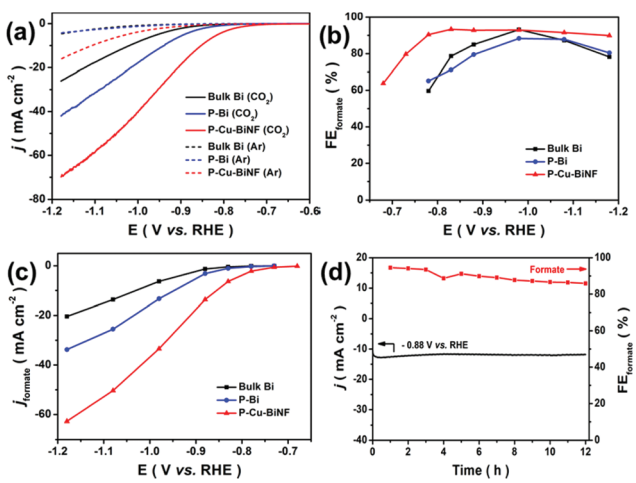

Fig. 4 CO_2RR performances of P–Cu–BiNF, P–Bi and bulk Bi measured in 0.5 M $KHCO_3$ electrolyte. (a) LSV curves collected under Ar or CO_2 atmosphere at a scan rate of 10 mV s^{-1}; potential-dependent (b) $FE_{formate}$ and (c) $j_{formate}$; (d) long-term stability test of P–Cu–BiNF at −0.88 V for 12 h.

Furthermore, potentiostatic electrolysis at the designated potentials from −0.68 to −1.18 V was conducted to analyse the generated gaseous and liquid products, and the corresponding chronoamperometric curves are presented in Fig. S8a–c.† Based on the results obtained from gas chromatography (GC) and nuclear magnetic resonance (NMR) spectra, H_2, CO and formate were the only detected products. As shown in Fig. 4b and S8d–f,† formate is the dominant product. The measured onset potential for formate production over P–Cu–BiNF was about −0.68 V, corresponding to the overpotential of about 450 mV,[43] which is much smaller than those of P–Bi and bulk Bi. When the applied overpotential was increased, the faradaic efficiency of formate ($FE_{formate}$) for P–Cu–BiNF sharply increased to 93.3% at −0.83 V, and can be maintained exceeding 90% in an impressively wide potential window from −0.78 to −1.18 V. By contrast, P–Bi and bulk Bi can only maintain the high $FE_{formate}$ in a very narrow potential window, despite them possessing a similar maximum $FE_{formate}$ compared with P–Cu–BiNF. Moreover, as shown in Fig. 4c, P–Cu–BiNF can exhibit a much higher formate partial current density ($j_{formate}$) than those of P–Bi and bulk Bi at all tested potentials. Notably, the $j_{formate}$ of P–Cu–BiNF can reach 62.7 mA cm^{-2} at −1.18 V, which is about 1.9 and 3.0 times higher than those of P–Bi (33.7 mA cm^{-2}) and bulk Bi (20.4 mA cm^{-2}), further demonstrating the boosted CO_2RR performance *via* the generation of a 3D network porous structure and Cu decoration. Moreover, control experiments implied that the amount of introduced Cu will affect the CO_2RR performance of P–Cu–BiNF-*x*, including $FE_{formate}$ and $j_{formate}$ (Fig. 4 and S9†).

Meanwhile, in order to prove the interaction between Bi and Cu, the electrocatalytic performance of P–Cu was characterized (Fig. S10†). Compared with P–Cu and P–Bi, P–Cu–BiNF formed with the introduction of Cu has a larger current density and better selectivity for formate production. Although the main products over P–Cu are H_2 and formate, the combination of Cu and Bi can obviously improve $FE_{formate}$ and $j_{formate}$. This indicates that the interaction between Bi and Cu can significantly improve the activity and selectivity of the catalyst.

Besides, P–Cu–BiNF also exhibited glorious long-term electrolysis stability. As shown in Fig. 4d, it can hold a stable current density of about 12.0 mA cm^{-2} at −0.88 V, as well as a satisfactory $FE_{formate}$ (89.6%), during 12 h of continuous electrolysis. Characterizations including PXRD and Bi 4f XPS indicated that the structure of P–Cu–BiNF underwent *in situ* electrochemical reduction during electrocatalysis, which resulted in its structural reconstruction and better crystallinity, and thus its good electrolytic stability (Fig. S11†). This was also manifested by the HRTEM observation (Fig. S12†). SEM and TEM images demonstrate that the morphology of P–Cu–BiNF exhibits no obvious change after long-term electrolysis (Fig. S12†). As a result, the outstanding CO_2RR performance of P–Cu–BiNF, covering the high $FE_{formate}$ and $j_{formate}$ and stability in a wide potential window, makes it among the best Bi-

based electrocatalysts (*e.g.*, f-Bi_2O_3,[44] Au-Bi_2O_3,[45] *etc.*) toward electrochemical conversion of CO_2 to formate (Table S1†).

In addition, the benefits of the 3D porous network structure and Cu decoration to the much enhanced CO_2RR performance in P–Cu–BiNF were further explored. As shown in Fig. S13,† P–Cu–BiNF exhibits a similar Tafel slope compared with P–Bi, indicating that Cu decoration has little effect on the reaction kinetics. Meanwhile, the Tafel slopes over these samples are close to 118 mV dec^{-1}, implying that the rate-determining step for formate production should be the initial electron transfer.[37,46] Moreover, electrochemical impedance spectroscopy (EIS) was conducted to analyse the electron transfer behaviours during the CO_2RR process. The smallest semicircle diameter of P–Cu–BiNF depicted in Fig. 5a reflects the smallest charge-transfer resistance owing to its conductive network, which is beneficial to the rapid electron-transfer during the CO_2RR process.[47] Furthermore, the electrochemically active surface areas (ECSAs) of the samples were also investigated.[48] Their double-layer capacitances (C_{dl}) were firstly evaluated, which has a positive correlation with the ECSAs. It was apparently suggested in Fig. 5b and S14† that P–Cu–BiNF possesses a much higher ECSA than those of P–Bi and bulk Bi. Specifically, the calculated C_{dl} of P–Cu–BiNF is about 3.15 mF cm^{-2}, which is 3.28 and 19.69 times higher than those of P–Bi (0.96 mF cm^{-2}) and Bi (0.16 mF cm^{-2}), respectively. In addition, in order to gain accurate ECSAs of the samples, the ECSA was further measured by chronoamperometry according to the Cottrell equation (Fig. S15 and S18†).[49] The ECSAs of bulk Bi, P–Bi and P–Cu–BiNF were assessed to be 0.0044, 0.0048 and 0.032 cm^2, respectively. And the ECSAs of P–Cu–BiNF-0.5, P–Cu–BiNF and P–Cu–BiNF-10 with different Cu contents were 0.020, 0.032 and 0.0065 cm^2, respectively. These results show that P–Cu–BiNF has the largest ECSA. Consequently, the combination of the accelerated charge-transfer rate and much enlarged ECSA originating from the synergistic effect of the 3D porous network structure and Cu decoration endows P–Cu–BiNF with an impressive CO_2RR performance. Additionally, the CO_2RR performance of P–Cu–BiNF-*x* varied with the amount of introduced Cu, despite them sharing similar morphologies, which may be associated with their different degrees in the promotion of charge transfer and the exposure of active sites *via* the incorporation of different amounts of Cu (Fig. S14–18†).

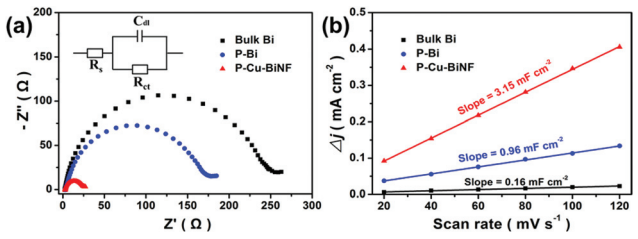

Fig. 5 (a) Electrochemical impedance plots and (b) capacitive Δj ($=j_a - j_c$) against scan rate for P–Cu–BiNF, P–Bi and bulk Bi.

4. Conclusions

In summary, a porous Cu-decorated Bi/Bi_2O_3 nanofoam as an efficient electrocatalyst was prepared for the first time *via* a facile fast-reduction method. Characterizations demonstrate that P–Cu–BiNF features a 3D porous network architecture composed of interconnected nanoparticles with a uniform size of around 15–20 nm. The incorporation of Cu into P–Cu–BiNF can regulate both the morphology and local electronic state of Bi/Bi_2O_3, which consequently much improves its CO_2RR performance. Remarkably, P–Cu–BiNF possesses a high faradaic efficiency exceeding 90% for CO_2-to-formate in a wide potential range from −0.78 to −1.08 V. Meanwhile, it can deliver a high formate partial current density (62.7 mA cm^{-2} at −1.18 V) and long-term stability. This work provides a Bi-based electrocatalyst for the high-efficiency conversion of CO_2-to-formate and also gives valuable guidelines for the development of efficient electrocatalysts for CO_2 reduction and other electrochemical syntheses.

Author contributions

Y. Z. and Q.-L. Z. conceived the research and designed the experiments. Y. Z. and C. C. carried out the synthesis, material characterizations and electrochemical measurements. Y. Z., C. C., X.-T. W. and Q.-L. Z. analysed the data and drafted the manuscript. All authors discussed and revised the manuscript.

Conflicts of interest

We declare that there are no conflicts of interest.

Acknowledgements

The authors are grateful for the financial support of the One Thousand Young Talents Program under the Recruitment Program of Global Experts, the National Natural Science Foundation of China (NSFC) (21901246 and 21905278), and the Natural Science Foundation of Fujian Province (2019J05158 and 2020J01116).

Notes and references

1 X. Li and Q.-L. Zhu, MOF-based materials for photo- and electrocatalytic CO_2 reduction, *EnergyChem*, 2020, **2**, 100033.
2 G. Centi, E. A. Quadrelli and S. Perathoner, Catalysis for CO_2 conversion: a key technology for rapid introduction of renewable energy in the value chain of chemical industries, *Energy Environ. Sci.*, 2013, **6**, 1711–1731.
3 D.-D. Ma, S.-G. Han, C. Cao, X. Li, X.-T. Wu and Q.-L. Zhu, Remarkable electrocatalytic CO_2 reduction with ultrahigh CO/H_2 ratio over single-molecularly immobilized pyrrolidi-

nonyl nickel phthalocyanine, *Appl. Catal., B*, 2020, **264**, 118530.
4 M. Aresta, A. Dibenedetto and A. Angelini, Catalysis for the Valorization of Exhaust Carbon: from CO_2 to Chemicals, Materials, and Fuels. Technological Use of CO_2, *Chem. Rev.*, 2014, **114**, 1709–1742.
5 D.-D. Ma, S.-G. Han, C. Cao, W. Wei, X. Li, B. Chen, X.-T. Wu and Q.-L. Zhu, Bifunctional single-molecular heterojunction enables completely selective CO_2-to-CO conversion integrated with oxidative 3D nano-polymerization, *Energy Environ. Sci.*, 2021, **14**, 1544–1552.
6 X. Zhu and Y. Li, Review of two-dimensional materials for electrochemical CO_2 reduction from a theoretical perspective, *Wiley Interdiscip. Rev.: Comput. Mol. Sci.*, 2019, **9**, e1416.
7 J.-M. Yan, S.-J. Li, S.-S. Yi, B.-R. Wulan, W.-T. Zheng and Q. Jiang, Anchoring and Upgrading Ultrafine NiPd on Room-Temperature-Synthesized Bifunctional NH_2-N-rGO toward Low-Cost and Highly Efficient Catalysts for Selective Formic Acid Dehydrogenation, *Adv. Mater.*, 2018, **30**, 1703038.
8 L. Peng, Y. Wang, I. Masood, B. Zhou, Y. Wang, J. Lin, J. Qiao and F.-Y. Zhang, Self-growing Cu/Sn bimetallic electrocatalysts on nitrogen-doped porous carbon cloth with 3D-hierarchical honeycomb structure for highly active carbon dioxide reduction, *Appl. Catal., B*, 2020, **264**, 118447.
9 X. Hou, Y. Cai, D. Zhang, L. Li, X. Zhang, Z. Zhu, L. Peng, Y. Liu and J. Qiao, 3D core–shell porous-structured Cu@Sn hybrid electrodes with unprecedented selective CO_2-into-formate electroreduction achieving 100%, *J. Mater. Chem. A*, 2019, **7**, 3197–3205.
10 X. Yu and P. G. Pickup, Recent advances in direct formic acid fuel cells (DFAFC), *J. Power Sources*, 2008, **182**, 124–132.
11 G. H. Gunasekar, K. Park, K.-D. Jung and S. Yoon, Recent developments in the catalytic hydrogenation of CO_2 to formic acid/formate using heterogeneous catalysts, *Inorg. Chem. Front.*, 2016, **3**, 882–895.
12 H. Zhong, Y. Qiu, T. Zhang, X. Li, H. Zhang and X. Chen, Bismuth nanodendrites as a high performance electrocatalyst for selective conversion of CO_2 to formate, *J. Mater. Chem. A*, 2016, **4**, 13746–13753.
13 S. Kim, W. J. Dong, S. Gim, W. Sohn, J. Y. Park, C. J. Yoo, H. W. Jang and J.-L. Lee, Shape-controlled bismuth nanoflakes as highly selective catalysts for electrochemical carbon dioxide reduction to formate, *Nano Energy*, 2017, **39**, 44–52.
14 J. H. Koh, D. H. Won, T. Eom, N.-K. Kim, K. D. Jung, H. Kim, Y. J. Hwang and B. K. Min, Facile CO_2 Electro-Reduction to Formate via Oxygen Bidentate Intermediate Stabilized by High-Index Planes of Bi Dendrite Catalyst, *ACS Catal.*, 2017, **7**, 5071–5077.
15 P. Deng, H. Wang, R. Qi, J. Zhu, S. Chen, F. Yang, L. Zhou, K. Qi, H. Liu and B. Y. Xia, Bismuth Oxides with Enhanced Bismuth–Oxygen Structure for Efficient Electrochemical Reduction of Carbon Dioxide to Formate, *ACS Catal.*, 2020, **10**, 743–750.
16 C. Cao, D.-D. Ma, J.-F. Gu, X. Xie, G. Zeng, X. Li, S.-G. Han, Q.-L. Zhu, X.-T. Wu and Q. Xu, Metal–Organic Layers Leading to Atomically Thin Bismuthene for Efficient Carbon Dioxide Electroreduction to Liquid Fuel, *Angew. Chem., Int. Ed.*, 2020, **59**, 15014–15020.
17 D. H. Won, C. H. Choi, J. Chung, M. W. Chung, E.-H. Kim and S. I. Woo, Rational Design of a Hierarchical Tin Dendrite Electrode for Efficient Electrochemical Reduction of CO_2, *ChemSusChem*, 2015, **8**, 3092–3098.
18 X. Zheng, Y. Ji, J. Tang, J. Wang, B. Liu, H.-G. Steinrück, K. Lim, Y. Li, M. F. Toney, K. Chan and Y. Cui, Theory-guided Sn/Cu alloying for efficient CO_2 electroreduction at low overpotentials, *Nat. Catal.*, 2019, **2**, 55–61.
19 M. Fan, S. Garbarino, G. A. Botton, A. C. Tavares and D. Guay, Selective electroreduction of CO_2 to formate on 3D [100] Pb dendrites with nanometer-sized needle-like tips, *J. Mater. Chem. A*, 2017, **5**, 20747–20756.
20 C. Kim, T. Möller, J. Schmidt, A. Thomas and P. Strasser, Suppression of Competing Reaction Channels by Pb Adatom Decoration of Catalytically Active Cu Surfaces During CO_2 Electroreduction, *ACS Catal.*, 2019, **9**, 1482–1488.
21 Z. B. Hoffman, T. S. Gray, K. B. Moraveck, T. B. Gunnoe and G. Zangari, Electrochemical Reduction of Carbon Dioxide to Syngas and Formate at Dendritic Copper–Indium Electrocatalysts, *ACS Catal.*, 2017, **7**, 5381–5390.
22 H. Shang, T. Wang, J. Pei, Z. Jiang, D. Zhou, Y. Wang, H. Li, J. Dong, Z. Zhuang, W. Chen, D. Wang, J. Zhang and Y. Li, Design of a Single-Atom Indiumδ+–N_4 Interface for Efficient Electroreduction of CO_2 to Formate, *Angew. Chem., Int. Ed.*, 2020, **59**, 22465–22469.
23 N. Han, M. Sun, Y. Zhou, J. Xu, C. Cheng, R. Zhou, L. Zhang, J. Luo, B. Huang and Y. Li, Alloyed Palladium–Silver Nanowires Enabling Ultrastable Carbon Dioxide Reduction to Formate, *Adv. Mater.*, 2021, **33**, 2005821.
24 Q. Gong, P. Ding, M. Xu, X. Zhu, M. Wang, J. Deng, Q. Ma, N. Han, Y. Zhu, J. Lu, Z. Feng, Y. Li, W. Zhou and Y. Li, Structural defects on converted bismuth oxide nanotubes enable highly active electrocatalysis of carbon dioxide reduction, *Nat. Commun.*, 2019, **10**, 2807.
25 J. Yang, X. Wang, Y. Qu, X. Wang, H. Huo, Q. Fan, J. Wang, L.-M. Yang and Y. Wu, Bi-Based Metal-Organic Framework Derived Leafy Bismuth Nanosheets for Carbon Dioxide Electroreduction, *Adv. Energy Mater.*, 2020, **10**, 2001709.
26 M. Y. Zu, L. Zhang, C. Wang, L. R. Zheng and H. G. Yang, Copper-modulated bismuth nanocrystals alter the formate formation pathway to achieve highly selective CO_2 electroreduction, *J. Mater. Chem. A*, 2018, **6**, 16804–16809.
27 G. L. De Gregorio, T. Burdyny, A. Loiudice, P. Iyengar, W. A. Smith and R. Buonsanti, Facet-Dependent Selectivity of Cu Catalysts in Electrochemical CO_2 Reduction at Commercially Viable Current Densities, *ACS Catal.*, 2020, **10**, 4854–4862.

28 H. Wang, Z. Liang, M. Tang, G. Chen, Y. Li, W. Chen, D. Lin, Z. Zhang, G. Zhou, J. Li, Z. Lu, K. Chan, T. Tan and Y. Cui, Self-Selective Catalyst Synthesis for CO_2 Reduction, *Joule*, 2019, **3**, 1927–1936.

29 W. Zhu, L. Zhang, S. Liu, A. Li, X. Yuan, C. Hu, G. Zhang, W. Deng, K. Zang, J. Luo, Y. Zhu, M. Gu, Z.-J. Zhao and J. Gong, Enhanced CO_2 Electroreduction on Neighboring Zn/Co Monomers by Electronic Effect, *Angew. Chem. Int. Ed.*, 2020, **59**, 12664–12668.

30 M. Xiao, Y. Chen, J. Zhu, H. Zhang, X. Zhao, L. Gao, X. Wang, J. Zhao, J. Ge, Z. Jiang, S. Chen, C. Liu and W. Xing, Climbing the Apex of the ORR Volcano Plot via Binuclear Site Construction: Electronic and Geometric Engineering, *J. Am. Chem. Soc.*, 2019, **141**, 17763–17770.

31 D.-D. Ma and Q.-L. Zhu, MOF-based atomically dispersed metal catalysts: Recent progress towards novel atomic configurations and electrocatalytic applications, *Coord. Chem. Rev.*, 2020, **422**, 213483.

32 L. Hou, J. Han, C. Wang, Y. Zhang, Y. Wang, Z. Bai, Y. Gu, Y. Gao and X. Yan, Ag nanoparticle embedded Cu nanoporous hybrid arrays for the selective electrocatalytic reduction of CO_2 towards ethylene, *Inorg. Chem. Front.*, 2020, **7**, 2097–2106.

33 D. Ren, J. Gao, L. Pan, Z. Wang, J. Luo, S. M. Zakeeruddin, A. Hagfeldt and M. Grätzel, Atomic Layer Deposition of ZnO on CuO Enables Selective and Efficient Electroreduction of Carbon Dioxide to Liquid Fuels, *Angew. Chem. Int. Ed.*, 2019, **58**, 15036–15040.

34 X. Shen, X. Liu, S. Wang, T. Chen, W. Zhang, L. Cao, T. Ding, Y. Lin, D. Liu, L. Wang, W. Zhang and T. Yao, Synergistic Modulation at Atomically Dispersed Fe/Au Interface for Selective CO_2 Electroreduction, *Nano Lett.*, 2021, **21**, 686–692.

35 Y. Xing, X. Kong, X. Guo, Y. Liu, Q. Li, Y. Zhang, Y. Sheng, X. Yang, Z. Geng and J. Zeng, Bi@Sn Core–Shell Structure with Compressive Strain Boosts the Electroreduction of CO_2 into Formic Acid, *Adv. Sci.*, 2020, **7**, 1902989.

36 L. Li, C. Tang, B. Xia, H. Jin, Y. Zheng and S.-Z. Qiao, Two-Dimensional Mosaic Bismuth Nanosheets for Highly Selective Ambient Electrocatalytic Nitrogen Reduction, *ACS Catal.*, 2019, **9**, 2902–2908.

37 C. Dai, Y. Qiu, Y. He, Q. Zhang, R. Liu, J. Du and C. Tao, Controlled synthesis of a Bi_2O_3–CuO catalyst for selective electrochemical reduction of CO_2 to formate, *New J. Chem.*, 2019, **43**, 3493–3499.

38 M. Zhao, Y. Gu, W. Gao, P. Cui, H. Tang, X. Wei, H. Zhu, G. Li, S. Yan, X. Zhang and Z. Zou, Atom vacancies induced electron-rich surface of ultrathin Bi nanosheet for efficient electrochemical CO_2 reduction, *Appl. Catal., B*, 2020, **266**, 118625.

39 D. Yao, C. Tang, L. Li, B. Xia, A. Vasileff, H. Jin, Y. Zhang and S.-Z. Qiao, In Situ Fragmented Bismuth Nanoparticles for Electrocatalytic Nitrogen Reduction, *Adv. Energy Mater.*, 2020, **10**, 2001289.

40 Y. Liang, W. Zhou, Y. Shi, C. Liu and B. Zhang, Unveiling in situ evolved In/In2O3-x heterostructure as the active phase of In2O3 toward efficient electroreduction of CO_2 to formate, *Sci. Bull.*, 2020, **65**, 1547–1554.

41 J. Di, J. Xia, M. F. Chisholm, J. Zhong, C. Chen, X. Cao, F. Dong, Z. Chi, H. Chen, Y.-X. Weng, J. Xiong, S.-Z. Yang, H. Li, Z. Liu and S. Dai, Defect-Tailoring Mediated Electron–Hole Separation in Single-Unit-Cell Bi3O4Br Nanosheets for Boosting Photocatalytic Hydrogen Evolution and Nitrogen Fixation, *Adv. Mater.*, 2019, **31**, 1807576.

42 D. Wang, Z.-N. Chen, Q.-R. Ding, C.-C. Feng, S.-T. Wang, W. Zhuang and L. Zhang, Rational Preparation of Atomically Precise Non-Alkyl Tin-Oxo Clusters with Theoretical to Experimental Insights into Electrocatalytic CO_2 Reduction Applications, *CCS Chem.*, 2020, **2**, 2607–2616.

43 N. Han, Y. Wang, H. Yang, J. Deng, J. Wu, Y. Li and Y. Li, Ultrathin bismuth nanosheets from in situ topotactic transformation for selective electrocatalytic CO_2 reduction to formate, *Nat. Commun.*, 2018, **9**, 1320.

44 T. Tran-Phu, R. Daiyan, Z. Fusco, Z. Ma, R. Amal and A. Tricoli, Nanostructured β-Bi_2O_3 Fractals on Carbon Fibers for Highly Selective CO_2 Electroreduction to Formate, *Adv. Funct. Mater.*, 2020, **30**, 1906478.

45 T. Tran-Phu, R. Daiyan, Z. Fusco, Z. Ma, L. Rahim, A. Kiy, P. Kluth, X. Guo, Y. Zhu, H. Chen, R. Amal and A. Tricoli, Multifunctional nanostructures of Au-Bi_2O_3 fractals for CO_2 reduction and optical sensing, *J. Mater. Chem. A*, 2020, **8**, 11233–11245.

46 W. Lv, J. Zhou, J. Bei, R. Zhang, L. Wang, Q. Xu and W. Wang, Electrodeposition of nano-sized bismuth on copper foil as electrocatalyst for reduction of CO_2 to formate, *Appl. Surf. Sci.*, 2017, **393**, 191–196.

47 C. Zhang, Z. Fu, Q. Zhao, Z. Du, R. Zhang and S. Li, Single-atom-Ni-decorated, nitrogen-doped carbon layers for efficient electrocatalytic CO_2 reduction reaction, *Electrochem. Commun.*, 2020, **116**, 106758.

48 H. Chen, J. Chen, J. Si, Y. Hou, Q. Zheng, B. Yang, Z. Li, L. Gao, L. Lei, Z. Wen and X. Feng, Ultrathin tin monosulfide nanosheets with the exposed (001) plane for efficient electrocatalytic conversion of CO_2 into formate, *Chem. Sci.*, 2020, **11**, 3952–3958.

49 H. Liang, S. Zhao, X. Hu, M. Ceccato, T. Skrydstrup and K. Daasbjery, Hydrophobic Copper Interfaces Boost Electroreduction of Carbon Dioxide to Ethylene in Water, *ACS Catal.*, 2021, **11**, 958–966.